

## Full Length Article

# On the study of the preparation of graphene-anchored NHC-iridium catalysts from a coke-like waste with application in water splitting

M. González-Ingelmo<sup>a</sup>, P. Álvarez<sup>a,\*</sup>, M. Granda<sup>a</sup>, V.G. Rocha<sup>a</sup>, Z. González<sup>a</sup>, U. Sierra<sup>b</sup>, B. Sánchez-Page<sup>c</sup>, M.V. Jiménez<sup>c,\*</sup>, J.J. Pérez Torrente<sup>c</sup>, J. Blasco<sup>d</sup>, G. Subias<sup>d</sup>

<sup>a</sup> Instituto de Ciencia y Tecnología del Carbono, INCAR-CSIC, C/Francisco Pintado, Fe, 26, Oviedo, Spain

<sup>b</sup> Centro de Investigación de Química Aplicada (CIQA) Laboratorio Nacional de Materiales Grafénicos, Boulevard Enrique Reyna 140, San José de los Cerritos, C.P. 25294 Saltillo, Coahuila, Mexico

<sup>c</sup> Instituto de Síntesis Química y Catálisis Homogénea, ISQCH, CSIC-Universidad de Zaragoza, Spain

<sup>d</sup> Instituto de Nanociencia y Materiales de Aragón, INMA, CSIC-Universidad de Zaragoza, Spain



## ARTICLE INFO

## Keywords:

Coke-like waste  
Graphene  
Diazonium electrografting  
Hybrid materials  
Water oxidation  
OER  
Green hydrogen production

## ABSTRACT

Graphene oxide has been prepared from an industrial coke-like waste. The morphology of this material (GO-CW) is similar to that of standard graphene oxide (GO-G), although its surface has more defects. Both materials were used to prepare hybrid NHC-Ir(I)/graphene materials, consisting of molecular Ir(NHC) complexes covalently anchored to the graphene surface through the NHC moiety, following two different synthetic routes: (a) direct graphene electrografting of the previously synthesized aniline-functionalized imidazole-2-ylidene-Ir(I) complex, and (b) a two-step sequence comprising initial electrografting of aniline-imidazolium salts and subsequent chemical reaction with Ir(I) precursor anchoring imidazole-2-ylidene-Ir(I) molecular complexes. The synthesized NHC-Ir/graphene hybrid catalysts are active in the oxygen evolution reaction (OER) resulting in current densities in a similar range to those of other NHC-iridium(I) catalysts supported on GO. The highest activity corresponds to hybrid catalysts prepared by the two-step route, with even higher activity and stability when graphene oxide from industrial waste is used. EXAFS spectra of the materials prepared from both synthesis routes before oxidation catalysis reveal the local Ir coordination shell and a structural interaction between Ir and graphene. Both XANES and EXAFS spectra after electrocatalysis point to more oxidized species in which the molecular nature of the iridium catalysts is preserved.

## 1. Introduction

Global energy demand is continuously increasing due to the increase of both the economy and the world's population growth [1]. This is leading to climate change that needs to be urgently reversed by transforming the traditional industrial sector, moving it towards a decarbonization scenario. This is the case of the well-established energy intensive industry for the production of steel, which needs to face the environmental issues while ensuring its current production. A possible solution to this problem passes through the minimization of the environmental impact in the coke production [2,3], feedstock material used for the iron production in the blast furnace. Among the several strategies that can be proposed for this purpose, we focus herein on valorizing one of the main residues generated during the coking battery process: a carbonaceous waste usually formed at the inner top section of this type

of oven. This material must be scrapped after several cycles of the oven usage and represents a serious environmental problem [4]. Its industrial characterization showed that this material has only certain characteristics similar to those of metallurgical coke. For this reason, this material is considered a waste residue, which is outdoor stored causing contamination in the surroundings. One of the most interesting ways to minimize the negative environmental impact of this residue is by transforming it into an advanced carbon nanomaterial such as graphene. Graphene is a nanomaterial with unique properties such as thermal stability or high electrical and thermal conductivity [5,6], with potential application in different environmental and energy applications [7–12]. Furthermore, graphene oxide, GO, prepared typically from graphite or even from other pregraphitic materials such as cokes [13], shows a single-layer oxidized graphenic structure with various oxygen-containing functionalities, such as alcohols, epoxy or acid groups. This

\* Corresponding authors.

E-mail addresses: [par@incar.csic.es](mailto:par@incar.csic.es) (P. Álvarez), [vjimenez@unizar.es](mailto:vjimenez@unizar.es) (M.V. Jiménez).

<https://doi.org/10.1016/j.apsusc.2024.159556>

Received 15 December 2023; Received in revised form 23 January 2024; Accepted 29 January 2024

Available online 2 February 2024

0169-4332/© 2024 The Author(s). Published by Elsevier B.V. This is an open access article under the CC BY-NC-ND license (<http://creativecommons.org/licenses/by-nc-nd/4.0/>).

can be used to develop fine chemistry on the surface and prepare hybrid materials for advanced applications [14–17].

One of them is the green hydrogen production by water splitting (energy vector) [18,19]. This process is a crucial electrochemical reaction to produce sustainable hydrogen directly from water [20,21]. The bottleneck of this process is the oxygen evolution half-reaction (OER) due to its large overpotential and slow kinetics [22,23]. Additionally, one of the major challenges in OER research is obtaining cost-effective electrodes without compromising their activity and durability/long-term performance [24–28].

The use of a catalyst is required for these type of reactions. Iridium and ruthenium are among the most efficient catalysts for OER [29–31]. Among these, homogeneous catalysts based on these metals exhibit certain advantages, as for example a high efficiency and more tunable structures, than heterogeneous systems such as metal oxides, (oxy)sulphides, (oxy)nitrides or metal (oxy)nanoparticles [32–34]. However, the immobilization of the homogeneous catalysts is required for their large-scale utilization, since it substantially improves their recyclability, reduces the amount of catalyst, enhances their efficiency and robustness, and prevents deactivation via associative intermolecular pathways [35–37].

The use of carbon nanomaterials, such as graphenes, as proactive catalyst support has been actively investigated because of their outstanding properties, including electrical conductivity, mechanical stability, tunable morphology, and functionality [38–41]. Particularly, graphene contributes to enhance electrocatalysts dispersions, optimizing the physicochemical properties of the catalyst, such as electronic structure or charge transfer rate for instance. These properties are maximized when the catalysts are covalently immobilized onto the graphene surface. This strategy involves a thorough control of the graphene surface properties as well as the establishment of precise synthetic procedures for the formation of hybrid graphene/metal materials, ensuring an adequate chemical environment for the monoatomic catalyst and interaction with the graphene. To achieve that, the use of graphene with controlled characteristics and high purity (low ash content and consistent crystalline structure) is highly recommended.

Graphenes are usually obtained from graphite [42–47] or even other fossils with controlled characteristics such as commercial pre-graphitic materials [13,48]. In all cases the composition and structure of these precursors are consistent and well-controlled since all these products are from natural resources (natural graphite) or synthetic commercial substances (synthetic graphite, coke). This offers the possibility to control the composition and structural properties of the graphenes prepared from them by selecting the oxidation/reduction methods or by adequate selection of the crystallinity of the parent graphite [49–51]. The final properties can therefore be modulated which, in catalytic applications, favors their proactive effect as supports in multiple catalytic systems [52,53], including covalently attached Ir compounds for OER reactions [37,54].

Replacing graphite (a strategic material) with an industrial coke-like waste as a raw material for the production of graphene oxide has environmental and economic benefits. This is the case of recent works describing the use of industrial wastes as graphene precursors, such as spent cathode carbon (SCC), hazardous waste unavoidably generated from aluminum electrolysis production [55]. However, when a residual waste (such as the material obtained from the inner top section of a coking oven) is used for this purpose, this control over the graphene surface could be difficult to achieve due to its heterogeneity and metal-based impurity content, which limits its future application, especially for fine chemistry.

The aim of this study is to develop efficient routes to immobilize molecular catalysts on the graphene surface made from carbonaceous waste to prepare hybrid materials for electrodes in hydrogen production by electrocatalytic water splitting. With that in mind we initially describe, for the first time, the preparation of graphene oxide (GO) from an industrial coke-like waste from the scrapping of the ovens used to

prepare coke for the blast furnace. It was prepared by means of the chemical route by introducing some adjustments due to the inherent presence of impurities. The characteristics of this material have been determined and compared to those of a reference standard GO prepared following the same procedure. The effect of these structural characteristics on the reactivity of the waste-based graphenes has been evaluated by defining different chemical routes to prepare new hybrid NCH-Ir(I)/graphene materials for electrocatalytic water oxidation. In particular, we have conducted two different synthetic routes for the covalent anchoring of Ir(I)-NHC complexes based on the electrografting methodology: (a) direct graphene electrografting of the previously synthesized imidazolium-Ir(I) complex making use of aryl diazonium salt chemistry [56], and (b) a two-step sequence comprising initial electrografting of the imidazolium ligand and subsequent chemical reaction with the appropriate Ir(I) precursor. The full characterization of the hybrid catalyst and the study of their catalytic performance in the OER reaction is reported, which allows determining the structural changes promoted in the catalyst by their different sequential preparation procedure and their relationship with their catalytic OER activity.

## 2. Experimental

### 2.1. General considerations

The iridium starting material  $[\text{Ir}(\mu\text{-Ome})(\text{cod})]_2$  was prepared according to the literature method [57]. Solvents were distilled immediately prior to use from the appropriate drying agents or obtained from a Solvent Purification System (Innovative Technologies).  $\text{CDCl}_3$  and  $\text{CD}_3\text{OD}$  were purchased from Euriso-top and used as received. The raw materials used in this work as graphene oxide precursors were an industrial coke-like waste (supplied by Industrial Minera México S.A. ( $<20\ \mu\text{m}$ )) obtained at  $2000\ ^\circ\text{C}$ , and a standard graphite ( $<20\ \mu\text{m}$ ) (supplied by Sigma-Aldrich).

### 2.2. Graphene oxides preparation from industrial coke-like waste (GO-CW) or from graphite oxides (GO-G)

Graphite oxides aqueous suspensions were prepared by a modified Hummer's method previously reported [13,58,59]. This method consists in the chemical oxidation of graphite to graphite oxide making use the Hummer's reagents and additional amounts of  $\text{NaNO}_3$  and  $\text{KMnO}_4$ . 360 mL of concentrated  $\text{H}_2\text{SO}_4$  were slowly added for a period of 2 h to a flask containing the raw carbon-based material (7.5 g) and  $\text{NaNO}_3$  (7.5 g). Once the mixture was homogeneous and stable, 45 g of  $\text{KMnO}_4$  were added in small doses and an ice bath was used to keep the temperature below  $20\ ^\circ\text{C}$ . The suspension was then heated at  $35\ ^\circ\text{C}$  and stirred for 3 h. After this time, 1.5 L of 3 %  $\text{H}_2\text{O}_2$  were slowly added and stirred for an additional 30 min. The mixtures were centrifugated at 3700 rpm for 30 min and the obtained solids were washed with deionized water and centrifugated again until neutral pH. Then, the obtained aqueous suspensions were sonicated for 8 h in an ultrasound bath. The obtained graphene oxide samples (GO) were labelled as **GO-CW** if the raw material came from the coke-like waste at  $2000\ ^\circ\text{C}$ , and **GO-G** if the raw material came from standard graphite.

### 2.3. Synthesis of $[(4\text{-NH}_2(\text{C}_6\text{H}_4)\text{HImMe})\text{Ir}(\text{I})]$ (LI)

The imidazolium salt 1-(4-aminophenyl)-3-methyl-imidazolium iodide was prepared from 1-(4-aminophenyl)imidazole.  $[4\text{-NH}_2(\text{C}_6\text{H}_4)\text{Im}]$  (500 mg, 3.14 mmol) was dissolved in 30 mL of acetonitrile and iodomethane (0.25 mL, 4.082 mmol) was added as the alkylating agent. The mixture was stirred at room temperature for 24 h, and the white solid was filtered, washed with  $\text{Et}_2\text{O}$  (3 x 4 mL) and dried under vacuum. Yield: 766 mg, 81 % (white solid). Anal. Calcd. for  $\text{C}_{10}\text{H}_{12}\text{N}_3\text{I}$ : C, 39.88; H, 4.02; N, 13.95. Found: C, 39.90; H, 4.01; N, 14.02. HRMS (ESI+,  $\text{CH}_3\text{OH}$ ,  $m/z$ ): calcd for  $\text{C}_{10}\text{H}_{12}\text{N}_3$  174.1031  $[\text{M}]^+$ ; found, 174.1131

[M]<sup>+</sup>. <sup>1</sup>H NMR (300 Hz, 298 K, CD<sub>3</sub>OD, Fig. S4Fig.S4): δ 9.24 (s, 1H, NCHN, Im), 7.87, 7.70 (s, 2H, 1:1, =CH, Im), 7.35 (d, *J*<sub>HH</sub> = 9.0, 2H, H<sub>o</sub>, C<sub>6</sub>H<sub>4</sub>), 6.82 (d, *J* = 9.0, 2H, H<sub>m</sub>, C<sub>6</sub>H<sub>4</sub>), 4.01 (s, 3H, CH<sub>3</sub>). <sup>13</sup>C{<sup>1</sup>H}-APT NMR (75 MHz, CD<sub>3</sub>OD, 298 K, Fig. S5Fig. S5): δ: 151.7 (NCHN, Im), 130.5 (C<sub>ipso</sub> CNH<sub>2</sub>), 125.8 (C<sub>ipso</sub> CIm), 125.2, 123.1 (=CH, Im), 124.5 (C<sub>o</sub>, C<sub>6</sub>H<sub>4</sub>), 116.1 (C<sub>m</sub>, C<sub>6</sub>H<sub>4</sub>), 36.8 (CH<sub>3</sub>).

#### 2.4. Synthesis of [IrI(cod)(4-NH<sub>2</sub>(C<sub>6</sub>H<sub>4</sub>)ImMe)] (1)

1-(4-aminophenyl)-3-methyl-imidazolium iodide (100 mg, 0.331 mmol) and [Ir(μ-OMe)(cod)]<sub>2</sub> (109 mg, 0.165 mmol) were suspended in 5 mL of dry THF and stirred under Ar atmosphere for 18 h at room temperature. The resulting suspension was filtered and the red solution was concentrated until almost dry. The product was obtained as a yellow powder solid after the addition of 5 mL of cold hexane, washing with cold hexane (2 x 2 mL) and dried under vacuum. Yield: 177 mg, 89 % (yellow solid). Anal. Calcd. for C<sub>18</sub>H<sub>23</sub>IrN<sub>3</sub>: C, 36.00; H, 3.86; N, 7.00. Found: C, 36.18; H, 3.92; N, 6.95. HRMS (ESI+, MeOH, *m/z*): calcd for C<sub>18</sub>H<sub>23</sub>IrN<sub>3</sub>, 600.5285 [M]; found, 601.5315 [M + H]<sup>+</sup>. <sup>1</sup>H NMR (300 Hz, CDCl<sub>3</sub>, 298 K, Fig. S6-S9): δ 7.74 (d, *J*<sub>HH</sub> = 8.5 Hz, 2H, H<sub>o</sub>), 7.06 (d, *J*<sub>HH</sub> = 2.0 Hz, 1H, Im), 6.96 (d, *J*<sub>HH</sub> = 2.0 Hz, 1H, Im), 6.72 (d, *J*<sub>HH</sub> = 8.5 Hz, 2H, H<sub>m</sub>), 4.78, 4.65 (m, 2H, 1:1, CH cod), 3.97 (s, 3H, CH<sub>3</sub>), 3.82 (s, 2H, NH<sub>2</sub>), 2.98, 2.48 (m, 2H, 1:1, CH cod), 2.08, 1.88, 1.62, 1.27 (m, 8H, 2:2:2:2, CH<sub>2</sub> cod). <sup>13</sup>C{<sup>1</sup>H}-APT NMR (75 MHz, CDCl<sub>3</sub>, 298 K, Fig. S10): δ 179.6 (C<sub>NCHN</sub>), 146.1, 131.4 (C<sub>ipso</sub> CNH<sub>2</sub>, CIm), 114.4 (C<sub>o</sub> C<sub>6</sub>H<sub>4</sub>), 126.2 (C<sub>m</sub> C<sub>6</sub>H<sub>4</sub>), 121.8, 122.2 (=CH Im), 82.2, 81.4 (=CH cod, trans NHC), 54.9, 54.7 (=CH cod, trans Br), 38.6 (CH<sub>3</sub>), 33.9, 31.8, 30.7, 30.0 (>CH<sub>2</sub> cod).

#### 2.5. Preparation of working electrodes

300 μL of the aqueous GO suspensions previously prepared (GO-CW or GO-G, 2000 ppm) were drop-casted onto a graphite disk current collector, coating a surface of 1 cm<sup>2</sup> and dried at 60 °C (1 h). These electrodes were used as the working electrode of a three-electrode cell comprising a graphite rod and Ag/AgCl electrode as the counter and reference electrodes, respectively. A chronoamperometry technique at -1 V (vs Ag/AgCl) was applied for 30 min using 0.1 M KNO<sub>3</sub> as electrolyte to obtain the corresponding electrochemical reduced graphene oxide materials (rGO). After reduction, the electrode was thoroughly rinsed with Milli-Q water.

##### 2.5.1. Route a: Preparation of rGO-G@Ir(cod)-a-EC and rGO-CW@Ir(cod)-a-EC

This route consists in the direct functionalization of the rGO with compound [IrI(cod)(4-NH<sub>2</sub>(C<sub>6</sub>H<sub>4</sub>)ImMe)] (1) via diazonium salt electrografting. 1 (12.0 mg, 0.002 mmol) was first suspended into a 10 mL degassed HCl 0.1 M solution at 4 °C and NaNO<sub>2</sub> (27.6 mg, 0.4 mmol) was added just before grafting to prepare the electrolyte. The electrochemical setup was a three-electrode cell degassed with N<sub>2</sub> where the electrode with rGO prepared before was used as working electrode, and Ag/AgCl and a graphite rod as reference and counter electrode, respectively. The cell was kept at 4 °C during the reaction using an ice bath. The electrochemical grafting of the in-situ generated diazonium salt was performed by CV starting from 0.436 V vs Ag/AgCl to -0.764 V vs Ag/AgCl with a scan rate of 10 mV/s repeated five times. The electrodes were rinsed with Milli-Q water to remove any adsorbed species. These materials were labelled as rGO-G@Ir(cod)-a-EC and rGO-CW@Ir(cod)-a-EC depending on the parent graphite used.

##### 2.5.2. Route b: Preparation of rGO-G@Ir(cod)-b-EC and rGO-CW@Ir(cod)-b-EC

This route involves initially the incorporation of the imidazole-2-ylidene precursor ligand through electrografting of the imidazolium salt, followed by a chemical reaction with the iridium precursor to anchor the iridium molecular complex. In this case, a solution of the imidazolium salt [(4-NH<sub>2</sub>(C<sub>6</sub>H<sub>4</sub>)HImMe)]I (L1) (6 mg, 0.02 mmol) and

NaNO<sub>2</sub> (27.6 mg, 0.4 mmol) dissolved 10 mL of HCl 0.1 M was used as electrolyte in the electrografting process. The solution was placed in a degassed three-electrode cell with the rGO as working electrode and Ag/AgCl and graphite rod as reference and counter electrode, respectively. The diazonium salt in situ formed was grafted to the graphene oxide electrodes performing five CVs starting from 0.436 V vs Ag/AgCl to -0.764 V vs Ag/AgCl with a scan rate of 10 mV/s. The electrodes were rinsed with Milli-Q water to remove any adsorbed species. Then, the electrodes were immersed in a solution of 5 mg of the methoxy-Ir(I) dimer, [Ir(μ-OMe)cod]<sub>2</sub>, in 7 mL of anhydrous tetrahydrofuran (THF) under a nitrogen atmosphere with shaking. After 24 h of reaction at room temperature, the electrodes were washed with THF (2 x 7 mL) and Et<sub>2</sub>O (2 x 4 mL) and then dried at 100 °C. These materials were labelled as rGO-G@Ir(cod)-b-EC and rGO-CW@Ir(cod)-b-EC depending on the parent graphite used.

#### 2.6. Electrochemical measurements

To evaluate the catalytic performance towards oxygen evolution reaction (OER), cyclic voltammetry (CV) and linear sweep voltammetry to determine Tafel slope values were conducted in a teflon three-electrode cell at room temperature and under an inert atmosphere. A 0.1 M solution of perchloric acid was used as electrolyte (Fig. S11). The cell comprised of a working electrode with a surface area of 1 cm<sup>2</sup> (prepared in advance), a reference electrode of Ag/AgCl/3.5 M KCl, and a graphite rod as counter electrode. All the potentials were referenced to RHE, which enables comparison with other works. The stability of the electrodes under study was assessed through chronoamperometry (CA) experiments at 1.7 V for 1 h. Electrochemical impedance measurements (EIS) were also carried out on these electrodes to evaluate the R<sub>ct</sub> values. In the EIS experiments, a potential perturbation of 10 mV was applied within a frequency range spanning from 100 kHz to 100 mHz. The EIS measurements were acquired under a constant potential of 1.7 V vs. RHE, potential at which OER is assumed to occur.

#### 2.7. Specific equipment.

High-resolution transmission electron microscopy (HRTEM) images were obtained using a JEOL JEM-2100F transmission electron microscope, equipped with a field-emission-gun (FEG) and operating at 200 kV. Elemental analyses were carried out on a Perkin-Elmer 2400 Series-II CHNS/O micro-analyser or a LECO-CHNS-932 micro-analyser equipped with a LECO-VTF-900 furnace coupled to the micro-analyser.

X-ray photoemission spectroscopy (XPS) spectra were performed on a SPECS system operating under a pressure of 10<sup>-7</sup> Pa with a Mg Kα X-ray source. The functional groups in the graphene-based materials were quantified by deconvolution of the corresponding high-resolution XPS peaks using a peak analysis procedure that employs a combination of Gaussian and Lorentzian functions and a Shirley baseline [60]. The spectra did not require charge neutralization and were subsequently calibrated to the C1s line at 284.5 eV. The amount of iridium in the hybrid catalysts was determined by means of Inductively Coupled Plasma Mass Spectrometry (ICP-MS) in an Agilent 7700x instrument [61]. Raman spectroscopy was performed on a Renishaw 2000 Confocal Raman Microprobe using a 514.5 nm argon ion laser. Spectra were recorded from 750 to 3500 cm<sup>-1</sup>.

Room-temperature X-ray absorption spectroscopy (XAS) measurements at the Ir L<sub>3</sub>-edge were carried out using a Si (311) double crystal monochromator at the CLAES beamline [62] of the ALBA synchrotron facility (Barcelona, Spain). The energy resolution ΔE/E was estimated to be about 8 × 10<sup>-5</sup> at the Ir L<sub>3</sub>-edge and a pellet of Ir metal mixed with cellulose was measured for energy calibration. The extended X-ray absorption fine structure (EXAFS) spectra were analyzed using the ARTEMIS program [63], which makes use of theoretical phases and backscattering amplitudes calculated from FEFF6 code [64]. The fits were carried out in R space using a sinus window for filtering purposes.

Samples **rGO-CW@Ir(cod)-b-EC** and **rGO-CW@Ir(cod)-a-EC** were obtained by scratching from the electrodes, mixed with cellulose and pressed into a pellet. Due to the low concentration of Ir, the EXAFS spectra were measured in fluorescence mode using a multi-channel silicon drift detector. In contrast, **rGO-G@Ir(cod)-b-EC** could be measured in transmission mode after sample dilution with cellulose.

$^1\text{H}$  and  $^{13}\text{C}\{^1\text{H}\}$  NMR spectra were recorded on a Bruker Avance 300 on a Bruker AV-300 spectrometer (300.13 MHz) at room temperature in  $\text{CDCl}_3$  or  $\text{CD}_3\text{OD}$ . NMR chemical shifts are reported in ppm relative to tetramethylsilane and referenced to partially deuterated solvent resonances. Coupling constants ( $J$ ) are given in Hertz. NMR assignments are based on homo- and heteronuclear correlation spectroscopy. Electrospray mass spectra (ESI-MS) were recorded on a Bruker Esquire 3000 + spectrometer using sodium formate as reference.

### 3. Results and discussion

#### 3.1. Preparation and characterization of graphene oxide from a coke-like waste

The characteristics of the coke-like waste (CW) and the standard graphite G, used herein for comparative purposes, are summarized in Table S1. The carbon content in both samples is quite high (~99 wt%), as expected for a material of this kind. However, the ash content in the coke-like waste is much higher, (~11.4 wt% in CW compared to 1.9 wt% in G) [51]. This high ash content is due to the nature of the carbonaceous residue obtained by scraping the interior of the coking oven at regular intervals. The composition of the ash fractions is Al (45 wt%), Fe (39 wt%), Ca (13 wt%) and, at to a lesser extent, Mg (2 wt%) and Zn (0.5 wt%), as determined by ICP-MS.

The XRD parameters of both samples (Fig. S1, Table S1), exhibit the typical intense crystalline peak at  $26.5^\circ$  corresponding to the (002) plane. The interlayer distance increases from 0.336 nm for the graphite to 0.339 nm in CW, which is consistent with a less ordered graphite structure in the later [65].

Both materials were used to prepare graphene oxides (GOs) via a modified Hummers method [13,58]. The modification takes into account the high ash content in the CW material (which increases the reactivity of the process making it dangerous) and consists of adjusting the concentrations of the reactants (see experimental section), as well as using an ice bath and reducing the rate of reactive addition. In this way, ashes are eliminated during the processing. By means of this procedure, the graphite oxides were obtained (see Supplementary Material for SEM visualization, Fig. S2). The expanded structure allowed that, after ultrasonic exfoliation, single folded GO sheets are easily obtained in the

water dispersions of CW (GO-CW), as determined by TEM observations (Fig. 1). The morphology is also very similar to that of GO-G, confirming that a coke-like waste to be used as raw material for graphene oxides. Additionally, Raman spectra of GO-CW exhibit similar  $I_{\text{D}}/I_{\text{G}}$  ratio (0.96) than GO-G (0.93) (Fig. S3).

XPS analysis of the samples revealed differences in the graphene surface chemistry of GO-G and GO-CW (Fig. 2, Table 1). GO-G has a slightly higher atomic C/O ratio than GO-CW (2.4 vs 2.2 respectively), indicative of a higher degree of oxidation in the waste-derived graphene oxide. This effect is also reflected in its high-resolution XPS C1s spectra. Thus, although both samples show the typical bimodal distribution of a graphene oxide, the highest intensity in GO-CW is achieved for the 286.5 eV (C-O, accounting for 40.4 %, while in GO-G this value decreases to 33.0 %, Table 1), while the highest intensity in GO-G is for the  $\text{Csp}^2$  bonds at 284.5 eV (43.5 % against 33.5 % in GO-CW). The higher presence of defects in GO-CW is ascribed to its heterogeneous nature (industrial waste). To gain more information about the carbonaceous structure, the O1s spectra of both samples were deconvoluted into 3 main peaks: ~531.0 eV (O1, oxygen doubly bonded to aromatic carbon), ~532.0 eV (O2, oxygen singly bonded to aliphatic carbon) and ~533.4 eV (O3, assigned to oxygen singly bonded to aromatic carbon) [66–68]. The type and distribution of oxygen functional groups are similar in both samples, except that GO-CW materials show a greater number of oxygen single bonded to aromatic carbon, suggesting a change in the oxidation pathways in the aromatic carbonaceous structure of this waste-based graphene oxide.

#### 3.2. In-situ preparation of hybrid NHC-Ir(I)/graphene materials at the electrode for OER

The GOs were used to produce in situ the hybrid NHC-Ir(I)/graphene materials by means of two sequential procedures. These two chemical routes a and b are depicted in Fig. 3. In both cases, the first step is the electroreduction of the GOs onto the surface electrode, the differences being in subsequent steps. In route a, surface functionalization of graphene films was carried out with the previously synthesized aniline-imidazol-2-ylidene-Ir complex by electrografting through the in-situ generation of diazonium salt [56]. The hybrid materials **rGO-G@Ir(cod)-a-EC** and **rGO-CW@Ir(cod)-a-EC** were then obtained directly. In contrast, the route b comprises the initial electrografting of the imidazolium salt from the proper aniline-imidazolium salt and, in another step, the chemical reaction of this functionalized material with the methoxy-iridium(I)-cyclooctadiene dimer precursor anchoring the molecular NHC-Ir(cod) molecular complex to yield **rGO-G@Ir(cod)-b-EC** and **rGO-CW@Ir(cod)-b-EC**.

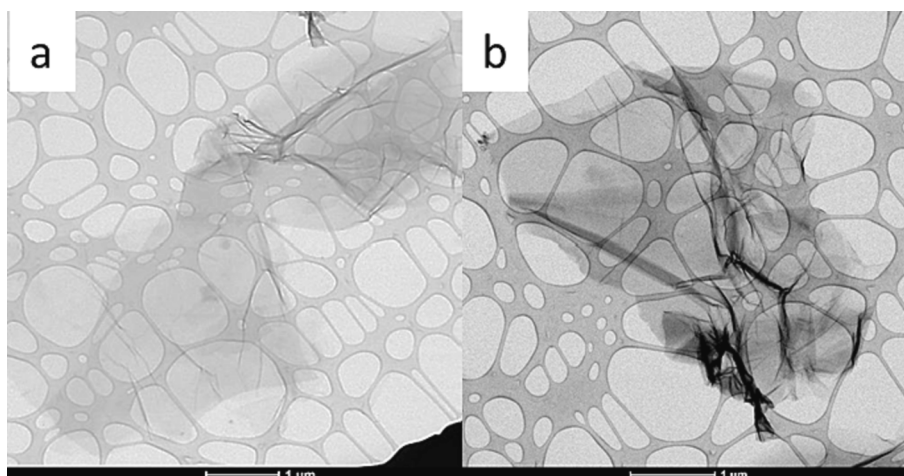


Fig. 1. TEM images of the graphene oxides obtained from (a) graphite (GO-G) and (b) coke-like waste (GO-CW).

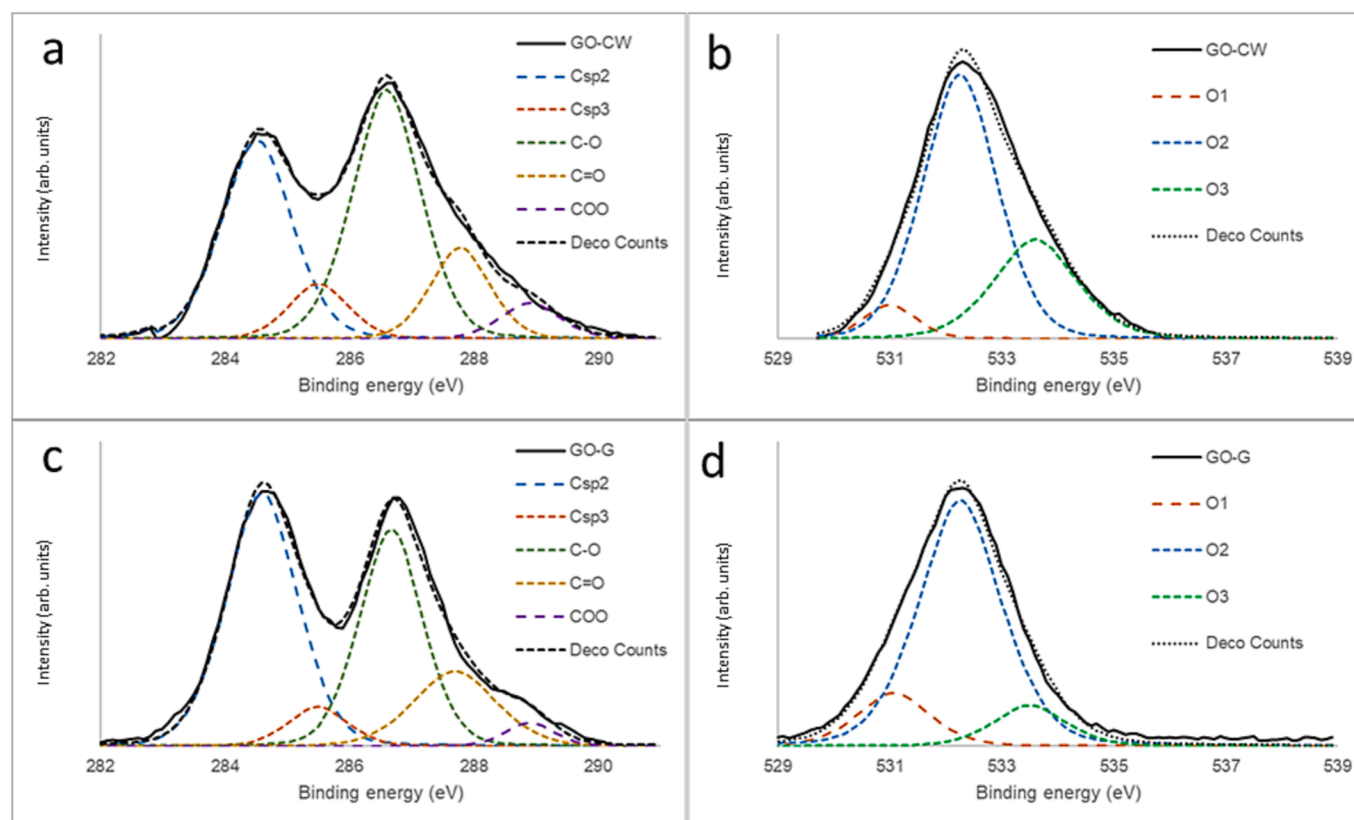


Fig. 2. XPS C1s (a, c) and O1s (b, d) curves of GO-CW (a, b) and GO-G (c, d).

Table 1

XPS Characterization of graphenes and hybrid materials prepared from G and CW.

Sample	C/O (%)	N (%)	Csp <sup>2</sup> (%)	Csp <sup>3</sup> (%)	C-O (%)	C=O (%)	COO (%)
GO-G	2.4	–	43.5	5.6	33.0	15.1	2.7
GO-CW	2.2	–	33.5	7.8	40.4	12.9	5.0
rGO-G@Ir(cod)-a-EC	6.2	2.1	73.8	10.0	10.8	2.9	2.6
rGO-CW@Ir(cod)-a-EC	6.5	2.0	71.1	14.3	10.2	2.5	1.8
rGO-G-N	6.9	5.0	69.1	15.1	8.2	4.8	2.8
rGO-CW-N	6.9	5.1	66.9	17.6	9.7	3.2	2.6
rGO-G@Ir(cod)-b-EC	7.0	2.4	78.0	14.8	3.2	2.6	1.4
rGO-CW@Ir(cod)-b-EC	7.0	2.3	76.2	15.3	3.8	4.2	0.6

SEM images of the electrodes prepared show that both methodologies lead to the formation of homogeneous films of the hybrid NCH-Ir/graphene materials in all cases (representative images for rGO-G@Ir(cod)-a-EC and rGO-CW@Ir(cod)-b-EC are depicted in Fig. 4a and 4b, respectively). The presence of iridium was not visualized but detected by EDX (Fig. 4d and S12). HRTEM images of all materials (representative images of rGO-G@Ir(cod)-b-EC and rGO-CW@Ir(cod)-a-EC are shown in Fig. 4e and 4f, respectively) confirmed the atomic size of the iridium which appears in these type of complexes as electron-dense regions with diameters from 0.2 to 0.7 nm [37,54]. The largest clusters visualized were previously reported to be formed during beam irradiation (spots or larger diameter) [69], which was also used to confirm the presence of iridium on the surface of the electrode. Moreover, EDX mapping of the TEM images confirms the homogeneous distribution of Ir along the graphene sheet (representative images corresponding to rGO-CW@Ir(cod)-a-EC as, Fig. 4c and d).

In order to gain information about the structure of the prepared hybrid materials, they were characterized by XPS. The hybrid materials prepared by the direct route a, rGO-G@Ir(cod)-a-EC and rGO-CW@Ir(cod)-a-EC, are quite similar. Their atomic composition (Table 1) is

consistent with the attachment of the NCH-Ir complex to the graphene surface, and both show similar Ir content (~1%), with the nitrogen content being almost double, as expected. The C/O content in these hybrid materials is higher in the hybrid materials compared to the parent GOs, suggesting a reduction of the oxygen functional groups during graphene processing (2.2–2.4 % in GOs vs 6.2–6.5 % in hybrid materials).

The high-resolution XPS curves of the elements derived from the attached iridium compound (N and Ir) are almost identical for the different carbon precursors. The Ir4f XPS spectra (Fig. 5a) show the characteristic doublet of Ir(I) species at ~ 62.2 and ~ 65.1 eV (corresponding to Ir4f7/2 and Ir4f5/2) [37,54,70]. The N1s XPS curves (Fig. 5b) appear as a single peak at ~ 400.6 eV, corresponding to the two nitrogen atoms of the imidazole-2-ylidene ligand [37]. The carbonaceous structure seems to be the main difference between the samples. On one hand, the XPS C1s curves of both hybrid materials show the decrease of the oxygen-containing functional groups (signal above ~ 286 eV) with respect to the parent GOs. This is mainly due to the electro-reduction process carried out prior to the electrografting of the Ir precursor. On the other hand, rGO-G@Ir(cod)-a-EC shows a slightly higher

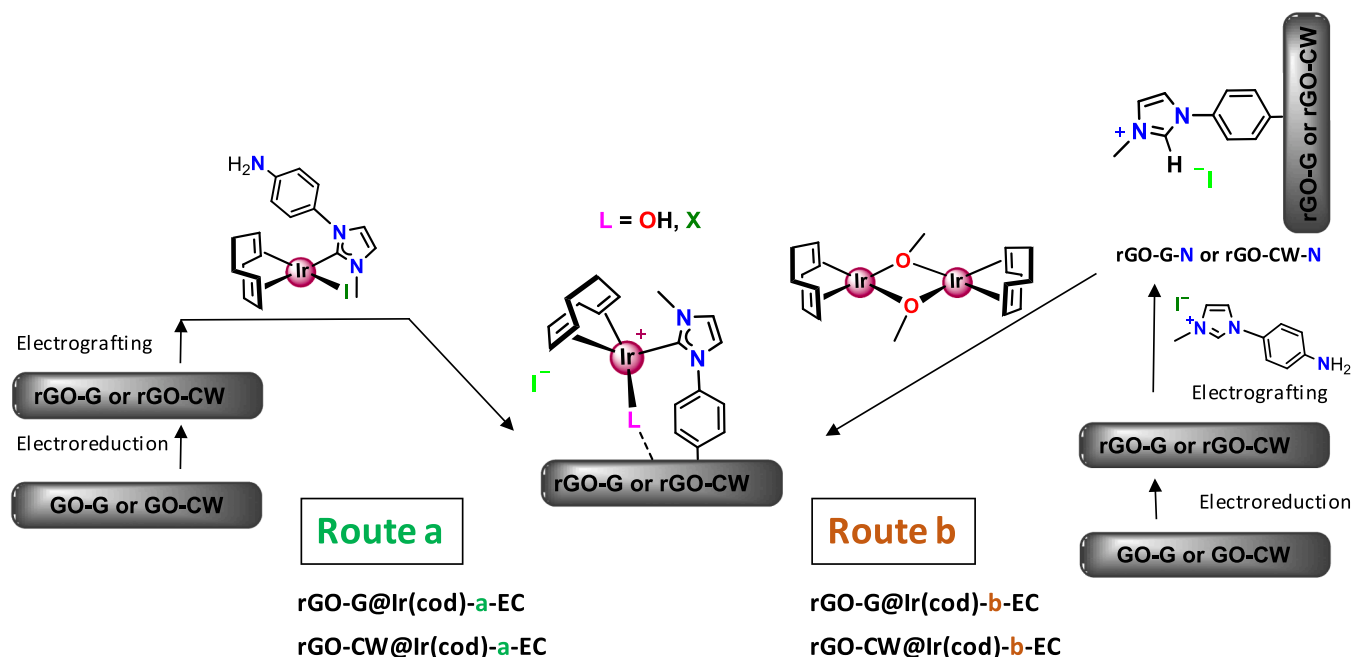


**Fig. 3.** Scheme of the two routes used to prepare the working electrodes based on imidazole-2-ylidene-Ir(I) complexes onto reduced graphene oxides prepared from a standard graphite (GO-G) or an industrial coke-waste (GO-CW).

contribution of the  $sp^2$  hybridized carbon atoms (73.8 % with respect to 71.1 % in **rGO-CW@Ir(cod)-a-EC**, Fig. 5c, d and Table 1), while **rGO-CW@Ir(cod)-a-EC** has a higher contribution of  $sp^3$  carbon atoms (14.3 % with respect to 10.0 % in **rGO-G@Ir(cod)-a-EC**). Since this trend is similar to that previously observed for the parent GOs, it could be explained here not only by the different degree of reduction during the GO processing but also as a consequence of the slightly larger number of structural defects in the carbonaceous structure of the graphene coming from the industrial waste. However, in contrast to what is observed for the GOs, the oxygen functional groups attached to the carbonaceous structure are similar in both samples, as observed in the O1s XPS spectra (Fig. 5d, f). This implies that the larger portion of oxygen singly bonded to aromatic carbon present in the parent GO-CW was preferentially electroreduced during processing.

The hybrid materials prepared by means of route b, as mentioned above, require the initial electrografting of the imidazolium ligand itself onto each type of electroreduced graphene oxide. These intermediates have been isolated and characterized by XPS (named **rGO-G-N** and **rGO-CW-N**, Fig. 6, Table 1). The atomic composition shows a  $\sim 5$  % of nitrogen, confirming the attachment of the N-ligand. Additionally, they exhibit higher C/O ratio than the parent GO-G and GO-CW ( $\sim 6.5$  vs  $2.2$  % in parent GOs), which is consistent with electroreduced graphene oxides. This electroreduction is seen in the C1s spectra of these intermediates as a reconstruction of the  $sp^2$  hybridized carbonaceous network (Fig. 6a, b). Again, the graphenic structure is larger in the case of the graphene prepared from graphite ( $Csp^2$  content of  $\sim 66$  vs  $\sim 69$  % in GO-CW-N). It is interesting to remark that the N1s spectra of the materials with the anchored imidazolium salt appear as a broad doublet with maxima at  $\sim 400.2$  and  $\sim 402.1$  eV, representative of the two nitrogen atoms in the 5-member ring of the heterocycle, each one with different atomic environment. This observation is similar to that previously observed by [37,71].

The linkage of the iridium molecular complex to the materials **rGO-G-N** and **rGO-CW-N** produces interesting results. Several points can be highlighted regarding the formation of the iridium complex. The support of the Ir(I) species is confirmed by the XPS Ir4f curves (Fig. 6g) appearance for both graphenes, since two doublets with maxima at the same position as those obtained for complexes prepared from route a

appear (Fig. 5a). The linkage of the iridium fragment to the NHC-moieties of both intermediate graphene materials is also confirmed by the transformation of their N1s curve, from the doublet in **rGO-G-N** and **rGO-CW-N** (Fig. 6c) to single narrower peaks with a maximum at  $\sim 400.6$  eV in **rGO-G@Ir(cod)-b-EC** and **rGO-CW@Ir(cod)-b-EC** (Fig. 6f). This narrowing is typical of the formation of a carbene moiety due to the linkage of the Ir complex to the in situ imidazole-2-ylidene ligand formed by the deprotonation of the anchored imidazolium [37]. It is noticeable that the same curves were obtained for the supported complexes that were formed via direct linkage to graphene, namely **rGO-G@Ir(cod)-a-EC** and **rGO-CW@Ir(cod)-a-EC** (Fig. 5b). All these facts suggest that the two synthetic routes proposed herein led to the formation of the same molecular iridium (I) complexes attached to the graphene materials. More importantly, the characterization of these hybrid materials confirms the possible utilization of coke-like wastes to develop graphene-based materials for fine chemistry. However, the use of this coke-like waste led to particular features in the carbonaceous structure of the graphene. The  $Csp^2$  content of **rGO-G@Ir(cod)-b-EC** and **rGO-CW@Ir(cod)-b-EC**, calculated from the XPS C1s curves (Fig. 6a, b, Table 1), is higher than that obtained for the graphene intermediates GO-G-N and GO-CW-N (76–78 % vs 67–69 %, respectively, Table 1). It is noteworthy that here the  $Csp^2$  ratio also accounts for the new C atoms introduced as Ir ligands, but even taking into account this fact, this content is also slightly higher than that obtained for the same complexes prepared by the direct route a (**rGO-G@Ir(cod)-a-EC** and **rGO-CW@Ir(cod)-a-EC**,  $\sim 71$ –74 % route a, Table 1). This trend is independent of the parent material of the graphene (graphite or industrial waste). We infer from the analysis of the XPS spectra that the electrografting process of small molecules (in this case, imidazolium salt) rather than with metal fragments (in this case, the NHC-Ir complex) seems to lead to a greater reconstruction of the graphene structure of the support itself.

### 3.3. Electrochemical performance of the NHC-Ir/graphene catalysts in the OER

The electrochemical performance in the OER of the hybrid NHC-Ir/graphene catalysts prepared by both methods was evaluated by cyclic voltammetry and the results obtained are summarized in Fig. 7.

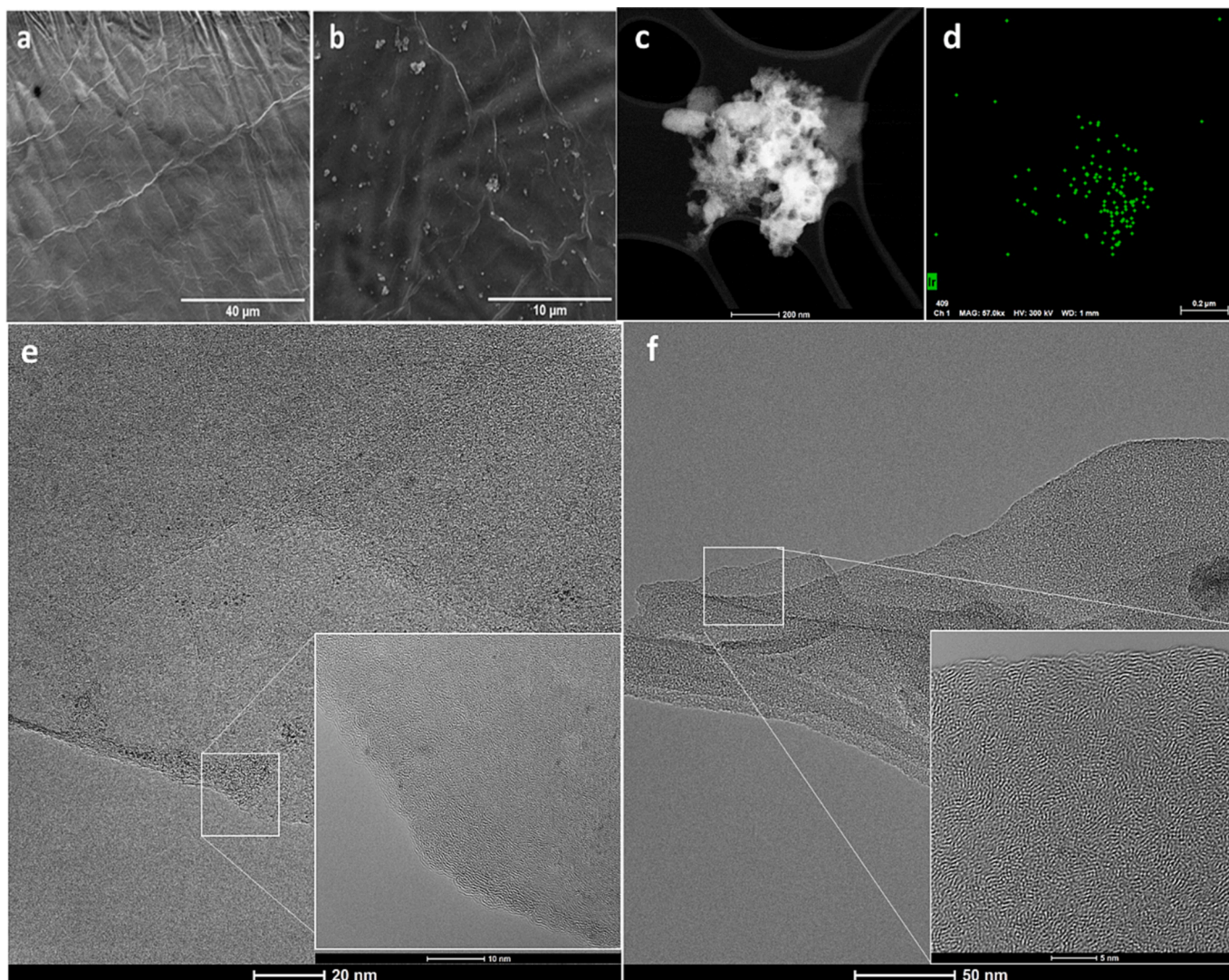


**Fig. 4.** Representative SEM images of the prepared electrodes: (a) **rGO-G@Ir(cod)-a-EC**, (b) **rGO-CW@Ir(cod)-b-EC**, (c) TEM and (d) EDX Iridium mapping of **rGO-CW@Ir(cod)-a-EC**. HRTEM representative images of: (e) **rGO-G@Ir(cod)-b-EC**, (f) **rGO-CW@Ir(cod)-a-EC**.

As it can be seen, irrespective of the synthetic route used, the electrodes studied showed electrocatalytic activity in the OER (CVs in the range of 0.3–2 V vs RHE at  $50 \text{ mVs}^{-1}$ ). The current densities obtained for the hybrid electrodes prepared from standard graphene in both methods, **rGO-G@Ir(cod)-a-EC** and **rGO-G@Ir(cod)-b-EC**, reach maximum values of  $25 \text{ mAcm}^{-2}$  in the first stabilized cycle (Fig. 7, a, b, solid blue lines). The current densities as well as the range are consistent with previous results related to the electrocatalytic activity in the OER of hybrid NHC-Ir(I) catalyst based on graphene oxides with similar chemical environment [54]. Interestingly, the hybrid electrodes based on a graphene material prepared from an industrial waste show an unusual behaviour. In the case of the first stabilized cycle for the waste-based hybrid catalyst prepared via route a (**rGO-CW@Ir(cod)-a-EC**), the current density decreases down to  $8 \text{ mAcm}^{-2}$  (Fig. 7, a, solid red line), which could be due to a different environment of the metallic catalyst itself, probably influenced by the type of support (graphene) used. In contrast, in the case of the waste-based hybrid material prepared via route b (**rGO-CW@Ir(cod)-b-EC**), the current density obtained in the first stabilized cycle under the same experimental conditions reaches values of  $33 \text{ mAcm}^{-2}$  (Fig. 7, b, solid red line), which is even higher than that obtained from an standard graphite (**rGO-G@Ir(cod)-b-EC**) (Fig. 7, b, solid blue line). The better results obtained for the waste-based hybrid material in comparison to standard graphite via

route b were also confirmed by a lower Tafel slope value, calculated from the LSV curves obtained at  $10 \text{ mVs}^{-1}$  (Fig. 7c). The Nyquist plot of the waste-based material, measured by Electrochemical impedance spectroscopy (EIS, Fig. S13) exhibit a lower diameter of the semicircle, evidencing also a better electron transfer rate. This points out that not only that graphene materials can be successfully prepared from an industrial waste and serves as an efficient OER catalysts supports, but also that the effectiveness of the proactive effect of the support in the catalyst is strongly dependent on the hybrid catalyst preparation method.

The stability of the prepared electrodes, other important parameter to consider, was measured herein by the CV curves obtained after 5 additional CV cycles of OER (Fig. 7, d, e, dashed lines). The current densities obtained for the electrodes from route a (**rGO-G@Ir(cod)-a-EC** and **rGO-CW@Ir(cod)-a-EC**, Fig. 7, d) are of  $\sim 10 \text{ mAcm}^{-2}$  much lower than the values obtained in the first cycle, particularly for **rGO-G@Ir(cod)-a-EC** (first cycle value of  $24 \text{ mAcm}^{-2}$ ) showing a very poor activity in the posterior stability test via chronoamperometric measurements (see Supplementary Material, Fig. S14). In contrast, the two hybrid electrodes prepared via route b (**rGO-G@Ir(cod)-b-EC** and **rGO-CW@Ir(cod)-b-EC**, Fig. 7, e) exhibit no substantial variation in the maxima current density obtained with respect to those shown in cycle 1. The chronoamperometric curves recorded at 1.7 V for 1 h confirms this stability (Fig. 7, f).

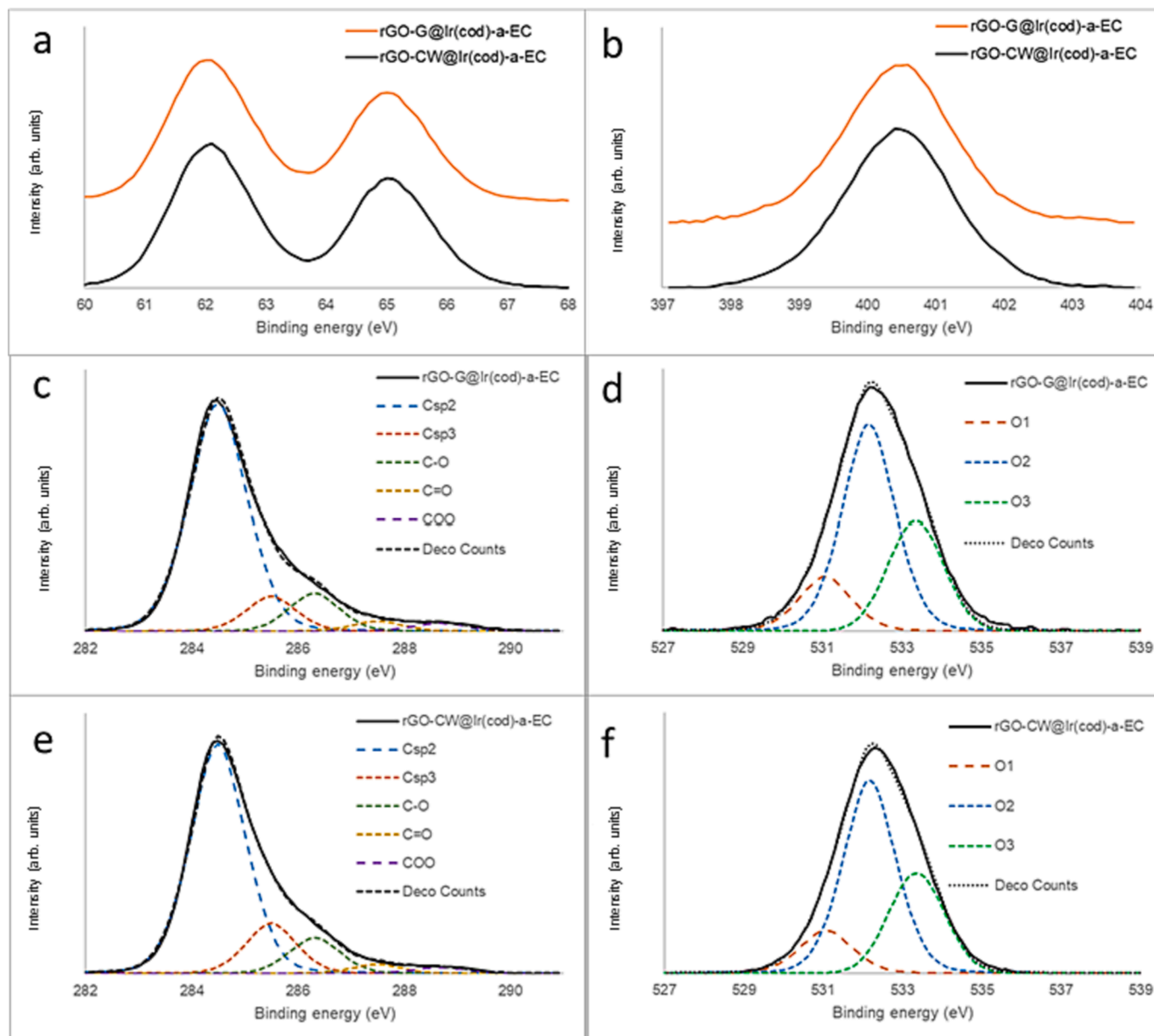


Fig. 5. XPS Ir4f (a), N1s (b), C1s (c, e) and O1s (d, f) curves of **rGO-G@Ir(cod)-a-EC** (a, b, c, d) and **rGO-CW@Ir(cod)-a-EC** (a, b, e, f).

A possible explanation for this lies in the fact that both material prepared via route b have a more aromatic carbonaceous support structure (higher content of C with  $sp^2$  hybridization, Table 1), which seems to exert a positive effect on the stabilization of the electrodes during the time studied. This beneficial effect in the catalyst stability should therefore be related to the selected synthetic procedure for the hybrid materials, highlighting the advantages of route b (multi-step) for the preparation of stable and effective graphene-anchored NHC-iridium electrodes for the OER. In this regard, we hypothesize that partial degradation of compound 1 could occur in the presence of the reactants required for diazonium salt electrografting (HCl/NaNO<sub>2</sub>). However, in the two-step route b, the imidazolium salt electrografting proceeds cleanly and therefore the anchoring of the Ir-NHC complexes is much more efficient.

The catalytic activity of these electrodes based on graphene materials might be more related to the local environment of Ir atom and its oxidation state, so the characterization of all these materials before and after the catalytic experiments was attempted by means of XAS measurements at the Ir-L<sub>3</sub> edge at room temperature (Fig. 8). For comparison

we analysed the hybrid materials samples before electrocatalysis **rGO-X@Ir(cod)-i-EC** ( $X = G, CW; i = a, b$ ) and the hybrid materials after 5 water oxidation electrocatalytic cycles **rGO-X@Ir(cod)I-PC** ( $X = G, CW; i = a, b$ ). The spectra are characterized by a strong resonance (or white line) at about 11219.5 eV whose intensity is higher for the post-electrocatalysis materials (PC) able to be measured. It is well known that dipolar transitions from the 2p core levels to unoccupied 5d state are the main contribution to this resonance and previous studies have correlated the area of the L<sub>3</sub> edge peak to the oxidation state of the Ir atom [72]. Therefore, according to the results obtained for the series **rGO-CW@Ir(cod)-a** and extrapolating to the rest of the series of this work, the XANES spectra (Fig. 8a) reveals a higher oxidation state of Ir in the material after electrocatalysis. This is in agreement with a higher oxidation state of the catalyst as active catalytic specie.

Fig. 8b compares the intensity of the L<sub>3</sub> peak for the two sets of electrode materials. We can clearly establish two groups. The pre-electrocatalysis materials **rGO-G@Ir(cod)-a-EC** and **rGO-CW@Ir(cod)-a-EC** and **rGO-CW@Ir(cod)-b-EC** exhibit a white line of similar intensity which can be considered as a prototype of Ir(I) compounds, as

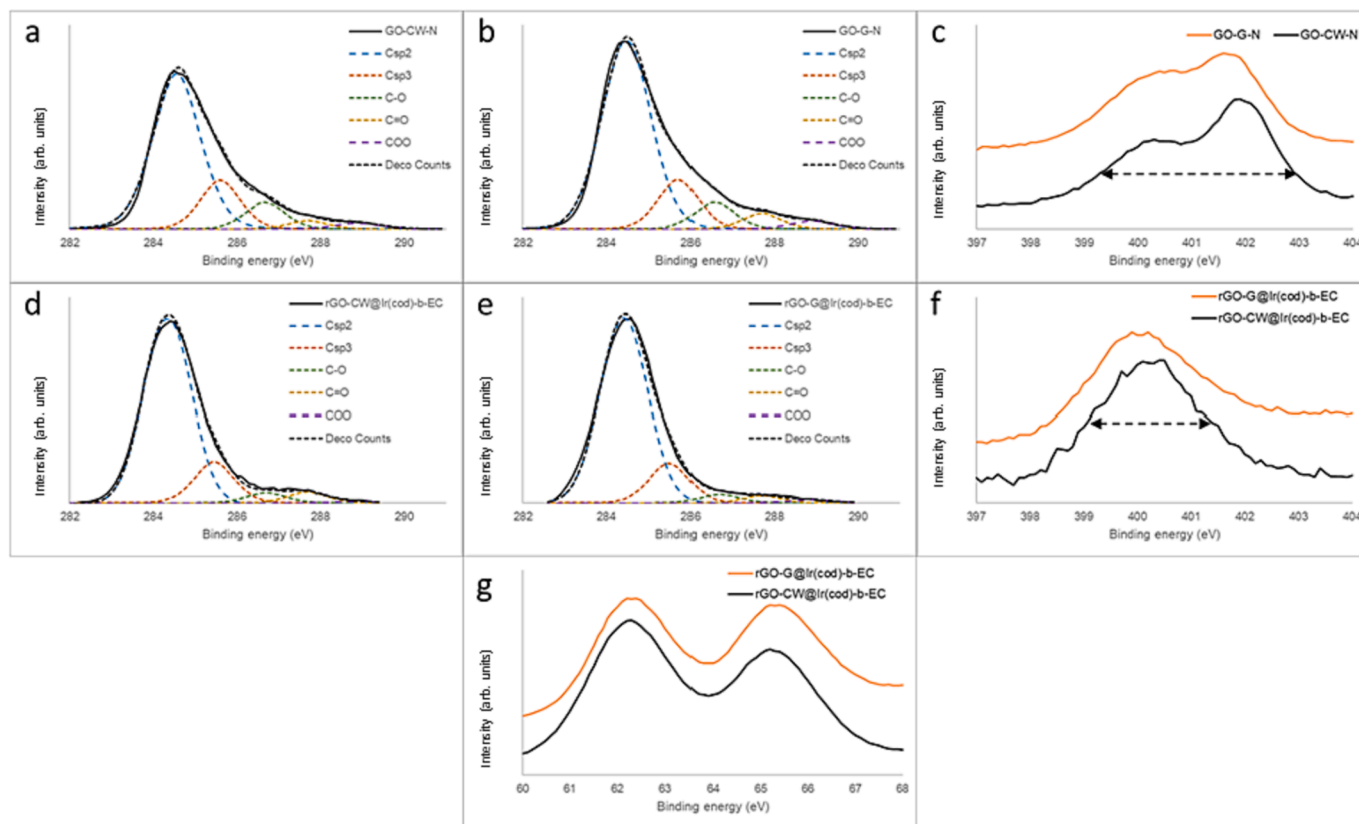


**Fig. 6.** High resolution XPS C1s (a, b, d, e), N1s (c, f) and Ir4f (g), of **rGO-CW-N** (a, c), **rGO-G-N** (b, c), **rGO-CW@Ir(cod)-b-EC** (d, f, g) and **rGO-G@Ir(cod)-b-EC** (e, f, g).

it is similar to **rGO-G@Ir(cod)-b-EC** that has been obtained by chemical synthesis by our known methods [54]. On the other side, the  $L_3$  peak intensity for the spectra of post-electrocatalysis materials **rGO-G@Ir(cod)-a-PC**, **rGO-CW@Ir(cod)-a-PC** and **rGO-CW@Ir(cod)-b-PC** is similar to the one for  $\text{IrO}_2$ , a reference for Ir(IV), although the latter has a slightly wider peak. These results support that Ir is oxidized to values close to Ir(IV) in the post-electrocatalysis materials obtained after five catalytic cycles.

The local environment of Ir atoms in the electrode materials was investigated using EXAFS spectroscopy. Unfortunately, it was not possible to obtain suitable measurement for **rGO-G@Ir(cod)-b-EC**. Additionally, the Ir content of these materials is very low, and although 16 measurements were made and averaged for each sample using a fluorescence detector with seven channels, the EXAFS oscillations,  $\chi(k)$ , vanished into noise for values of  $k > 10 \text{ \AA}^{-1}$ . The FTs are characterized by an intense peak at about  $1.6\text{--}1.8 \text{ \AA}$  (without phase shift correction), associated with the first coordination shell of Ir atoms (see Fig. 8c). No other intense peak at longer R, typical of Ir-I bonds is observed. This indicates that the Ir present in the precursor salts has been replaced by lighter elements. The FTs show clear differences between the different electrode materials. **rGO-CW@Ir(cod)-b-EC** shows its peak at a slightly smaller distance than **rGO-G@Ir(cod)-b-EC**, indicating longer bond lengths for the Ir atom in the second electrode material. Furthermore, significant differences are observed before and after the electrocatalytic water oxidation cycles. The post-electrocatalysis material, **rGO-CW@Ir(cod)-b-PC** shows a bigger peak than **rGO-CW@Ir(cod)-b-EC**. This is consistent with a less disordered coordination environment for Ir atoms in the post-electrocatalysis material.

Bearing in mind our previous experience with similar compounds [37,54], we have tried to use the modified crystallographic data of the  $[\text{Ir}(\text{NCCH}_3)(\text{cod})\{\text{MeIm}(\text{CH}_2)_3\text{OH}\}][\text{BF}_4]$  compound [73] to model the Ir(I) local structure in the pre-catalysis electrode materials as they are

expected to have a similar environment for the metal atom. The model followed implies that the Ir has a square planar coordination sphere formed by an imidazol-2-ylidene ring, a cyclooctadiene (cod) ligand and a nitrogen atom from the acetonitrile ligand in the reference compound. The modification herein consisted of replacing the nitrogen coordinated to the iridium with an oxygen (arising from oxygen-containing functional groups on the rGO surface) and thus, we can obtain theoretical phases and amplitudes for Ir-O and Ir-C scattering paths. This model works well for the three electrode materials studied.

The best fit results are summarized in Table 2. Due to the limited range in k-space, the fit was limited to the first coordination shell and several constrains were used. The four Ir-C distances to the cod ligand were reduced to the same value for both electrode materials. In the case of **rGO-CW@Ir(cod)-b-EC** and **rGO-CW@Ir(cod)-b-PC**, the Ir-C (imidazolium ring) and Ir-O bond lengths were equalized and then we refined the difference between the two groups of distances (a single parameter). Average inner potentials ( $\Delta E_0$ ) and Debye-Waller factors ( $\sigma^2$ ) were used for all paths. It is noteworthy that EXAFS analysis for **rGO-G@Ir(cod)-b-EC** was performed under the same conditions as the other two samples for the sake of comparison although the better quality of its data allows for fitting over a longer range (Fig. S15). The data of Table 2 confirm that the Ir bond lengths are a bit longer for **rGO-G@Ir(cod)-b-EC** (Fig. S15) than for **rGO-CW@Ir(cod)-b-EC** (Fig. S16). Moreover, the post-electrocatalysis material, **rGO-CW@Ir(cod)-b-PC** (Fig. S17), exhibits the shorter interatomic distances along with a lower  $\sigma^2$ -value. This suggests a higher oxidation state for Ir atoms in this electrode material but preserving the nearest local environment of the pre-electrocatalysis material.

The above results highlight the similarities that exist in the first coordination sphere for all the hybrid catalysts studied, regardless of the nature of the graphene support. On the one hand, the results also show that part of the oxygens from the residual oxygenated functional groups

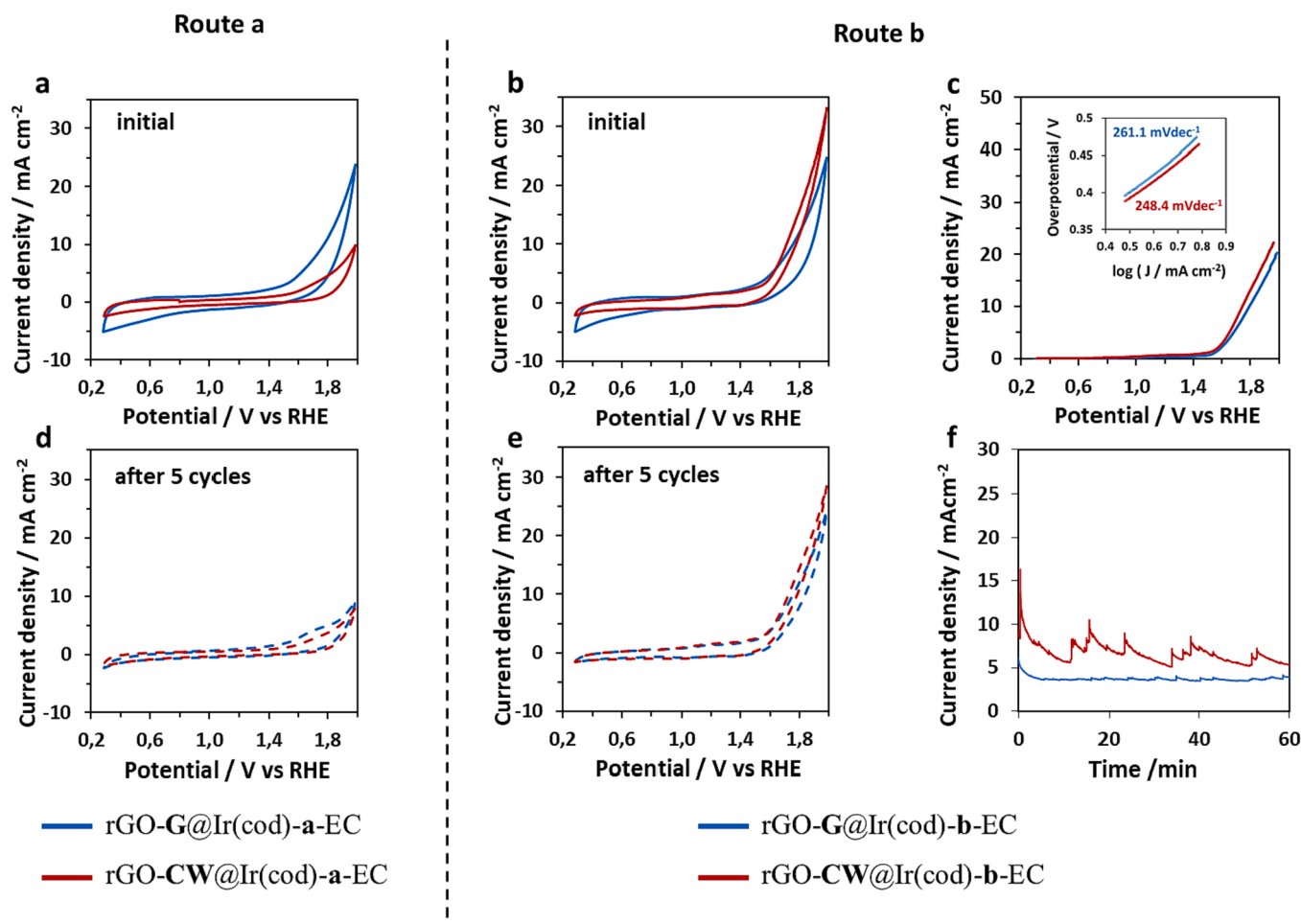


Fig. 7. Electrochemical characterization of the hybrid NHC-Ir/graphene materials based on graphite (G) or industrial waste (CW). Route a: rGO-G@Ir(cod)-a-EC and rGO-CW@Ir(cod)-a-EC, and Route b: rGO-G@Ir(cod)-b-EC and rGO-CW@Ir(cod)-b-EC: a, b, d, e) CV curves measured in the range of 0.3–2 V vs RHE at 50 mVs<sup>-1</sup> (Initial activity (higher level) and after five cycles (lower level)). c) LSVs measured in the electrodes from route b at 10 mVs<sup>-1</sup> in the potential range of 0.3–2 V vs RHE and the corresponding Tafel slope values (c, inset). f) CAs recorded on the electrodes from route b at 1.7 V for 1 h.

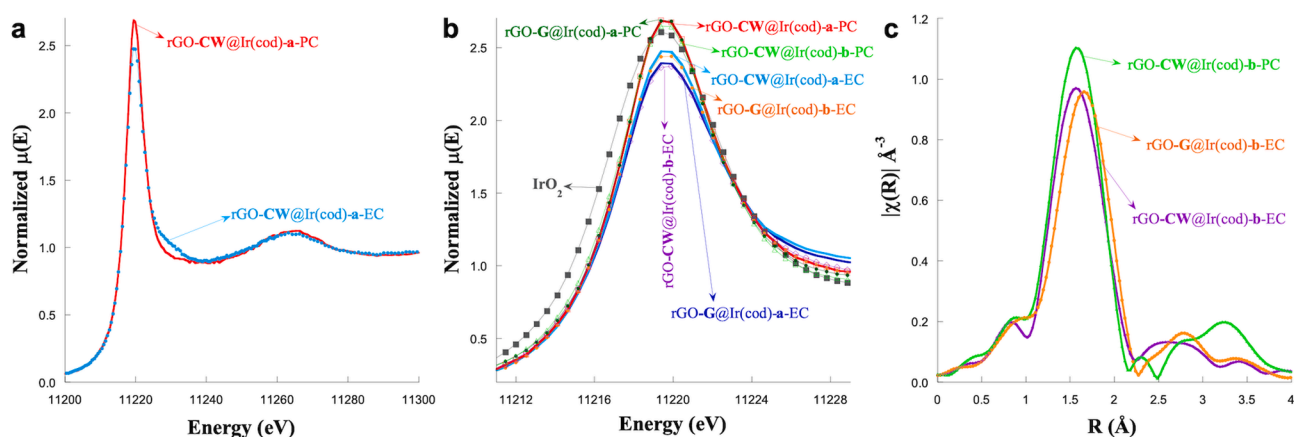


Fig. 8. (a) Normalized L<sub>3</sub> X-ray absorption edges for rGO-CW@Ir(cod)-a-PC (red line) and rGO-CW@Ir(cod)-a-EC (cyan circles) electrode materials. (b) Detail of the main resonance at the L<sub>3</sub> edge for the previous electrode materials (red and cyan), rGO-G@Ir(cod)-a-EC (blue), rGO-G@Ir(cod)-a-PC (dark green), rGO-CW@Ir(cod)-b-EC (purple), rGO-CW@Ir(cod)-b-PC (light green), rGO-G@Ir(cod)-b-EC (orange) and IrO<sub>2</sub> (grey). The two later materials can be considered as references for Ir(I) and Ir(IV) compounds, respectively. (c) Fourier transform (modulus) of the k<sup>2</sup>-weighted  $\chi(k)$  signals extracted using a sinus window between 2.5 and 10.5 Å<sup>-1</sup>, for rGO-G@Ir(cod)-b-EC (orange), rGO-CW@Ir(cod)-b-EC (purple), and rGO-CW@Ir(cod)-b-PC (light green). (For interpretation of the references to colour in this figure legend, the reader is referred to the web version of this article.)

**Table 2**

Refined inner potential ( $\Delta E_0$ ), interatomic distances and Debye-Waller factors ( $\sigma^2$ ) obtained from the best fits of the EXAFS spectra. The residual factor ( $R_F$ ) accounts for the misfit between the actual data and the theoretical calculations. Numbers in parentheses are the errors estimated in the last significant digits. The attenuation factors were fixed to 1 for all paths.

Sample	$\Delta E_0$ (eV)	Ir-C (Å)	Ir-O (Å)	$\sigma^2$ (Å <sup>2</sup> ) $\times 10^{-3}$	$R_F$
rGO-G@Ir(cod)-b-EC	6.0(14)	1 $\times$ 2.053(29)	1 $\times$ 1.937(29)	1.5(9)	0.006
		4 $\times$ 2.089(9)	-		
rGO-CW@Ir(cod)-b-EC	5.2(13)	1 $\times$ 2.009(12)	1 $\times$ 2.009(12)	3.1(7)	0.008
		4 $\times$ 2.076(12)	-		
rGO-CW@Ir(cod)-b-PC	5.1(21)	1 $\times$ 9.85(13)	1 $\times$ 1.985(13)	2.2(7)	0.008
		4 $\times$ 2.052(13)	-		

on the wall of the graphene supports also contribute to the first coordination sphere Ir, establishing an interaction with the support. On the other hand, taking into account the catalytic behaviour of these materials (Fig. 7), it seems clear that the carbonaceous structure of the support (graphene) exerts a critical influence on the overall electrocatalytic OER activity. Thus, a defective structure in graphene, such as that exhibited by graphene obtained from an industrial waste (GO-CW) (Table 2), requires some degree of reconstruction of its Csp<sup>2</sup> structure to exhibit a more pronounced proactive effect towards electrocatalytic OER, and the latter can be achieved by selecting an appropriate synthetic procedure, in this case a multi-step route.

#### 4. Conclusions

An industrial coke-like waste has been successfully used to prepare graphene oxides (GO-CW), similar to those obtained from a standard graphene used for comparative purposes (GO-G). Structural characterization of GO-CW (SEM, TEM XPS, EDX) shows that it exhibits a more carbonaceous defective surface than standard GO-G (obtained under the same experimental conditions) probably as a consequence of the heterogeneous composition to which the industrial waste was subjected. The obtained GOs have been used for the preparation of NHC-Ir/graphene hybrid materials by covalent support of Ir-NHC complexes on graphene through two different methodologies: direct electrografting of the 4-NH<sub>2</sub>-C<sub>6</sub>H<sub>4</sub>-NHC-iridium(I) precursor (route a) or through a two-step sequence comprising initial electrografting of the 4-aniline-imidazolium salt and subsequent chemical reaction with the Ir(I) precursor (route b). The prepared molecular graphene-anchored NHC-iridium electrodes resulted in active electrocatalysts in the OER. Therefore, this work demonstrates how an industrial coke-like waste, highly heterogeneous in its composition and with high amount of metal-based ashes, can be transformed into graphene oxides which can be successfully used as proactive supports of OER catalysts. The origin of the graphene support (which defines its surface characteristics) and the procedure of molecular NHC-Ir(I) complex anchorage are essential parameters related to OER performance (efficiency and stability), the two-step sequential route, route b, being the better methodology to obtain stable electrodes.

Structural characterization of the hybrid electrocatalysts (HRTEM, XPS) evidences differences particularly in their carbonaceous structure. EXAFS characterization of the electrode materials before the oxidation catalysis is in accordance with the proposed structures Ir-graphene, suggesting a square planar coordination sphere of the Ir formed by the NHC ligand, the cyclooctadiene diolefin and a hydroxyl or other oxygenated group on the graphene surface. The EXAFS spectra performed after the electrocatalytic OER cycles point to more oxidized species in which the molecular nature of the iridium catalysts is maintained. This reveals a long-term effect of the graphene structure on the catalysis, in which the presence of defects in the graphene layer enhances the proactive effect on the catalytic activity when a certain degree of reconstruction of the graphenic structure is achieved. In this regard, the two-step synthetic procedure, which leads to a higher reconstruction of the Csp<sup>2</sup> structure in the graphene surface, has a

positive effect on the catalyst stability in both hybrid materials and it is preferred for the preparation of highly stable catalysts.

#### CRediT authorship contribution statement

**M. González-Ingelmo:** Investigation, Methodology. **P. Álvarez:** Conceptualization, Funding acquisition, Supervision, Writing – original draft, Writing – review & editing. **M. Granda:** Writing – review & editing, Conceptualization. **V.G. Rocha:** Writing – review & editing. **Z. González:** Writing – review & editing. **U. Sierra:** Methodology, Investigation. **B. Sánchez-Page:** Investigation, Methodology. **M.V. Jiménez:** Conceptualization, Investigation, Methodology, Writing – original draft, Writing – review & editing. **J.J. Pérez Torrente:** Writing – review & editing, Funding acquisition. **J. Blasco:** Writing – review & editing, Formal analysis, Data curation. **G. Subias:** Data curation.

#### Declaration of competing interest

The authors declare the following financial interests/personal relationships which may be considered as potential competing interests: P. Álvarez reports financial support was provided by Spanish Ministry of Science and innovation (MICINN). J. J. Pérez-Torrente reports financial support was provided by Spanish Ministry of Science and innovation (MICINN). P. Álvarez reports financial support was provided by Spanish National Research Council (CSIC). J.J.Pérez-Torrente reports financial support was provided by Departamento de Ciencia, Universidad y Sociedad del Conocimiento del Gobierno de Aragón. V.G.Rocha reports financial support was provided by Spanish Government (Ramón y Cajal fellowship). M. González-Ingelmo reports financial support was provided by Asturias regional Government (FICYT). J. Blasco reports equipment, drugs, or supplies and travel were provided by ALBA synchrotron. If there are other authors, they declare that they have no known competing financial interests or personal relationships that could have appeared to influence the work reported in this paper.

#### Data availability

Data will be made available on request.

#### Acknowledgements

The authors thank the Spanish Ministry of Science and innovation (MICINN) (PID2019-104028RB-I00, PID2019-103965GB-I00 and PID2022-137208NB-I00), Spanish National Research Council-CSIC (icoop program, COOPB22006), and Departamento de Ciencia, Universidad y Sociedad del Conocimiento del Gobierno de Aragón (groups E42\_23R and E12\_23R) for their financial support. V.G. Rocha would like to thank the Spanish Government (Ramón y Cajal fellowship RYC2018-024404-I). M. González-Ingelmo acknowledges her fellowship from the Asturias regional Government (FICYT, Severo Ochoa Program BP20-168). Granted beam time at ALBA synchrotron is appreciated (proposal No. 2020024246).

## Appendix A. Supplementary data

Supplementary data to this article can be found online at <https://doi.org/10.1016/j.apsusc.2024.159556>.

## References

- N.S. Lewis, D.G. Nocera, Powering the planet: chemical challenges in solar energy utilization, *Proc. Natl. Acad. Sci. U.S.A.* 103 (2006) 15729–15735.
- T.V. Kiseleva, V.G. Mikhailov, I.G. Stepanov, Environmental and economic management of coke plants, *Steel Transl.* 48 (2018) 647–651.
- I.A. Sultanguzin, M.V. Isaevand, S.Y. Kurzanov, Optimizing the production of coke, coal chemicals, and steel on the basis of environmental and energy criteria, *Metallurgist* 54 (2011) 600–607.
- G. Diaz-Ignacio, Experimentación de la adsorción de un coque proveniente de una mina de carbón, (doctoral Dissertation) Universidad Nacional Autónoma De México. México (2018).
- A.K. Geim, K. Novoselov, The rise of graphene, *Nat. Mater.* 6 (2007) 183–191.
- C. Soldano, A. Mahmood, E. Dujardin, Production, properties and potential of graphene, *Carbon* 48 (2010) 2127–2150.
- R. Raccichini, A. Varzi, S. Passerini, B. Scrosati, The role of graphene for electrochemical energy storage, *Nat. Mater.* 14 (2015) 271–279.
- W.K. Chee, H.N. Lim, Z. Zainal, N.M. Huang, I. Harrison, Y. Andou, Flexible graphene-based supercapacitors: a review, *J. Phys. Chem. C* 120 (2016) 4153–4172.
- Z. González, C. Botas, P. Álvarez, C. Blanco, R. Santamaría, M. Granda, R. Menéndez, Thermally reduced graphite and graphene oxides in VRFBs, *Nano Energy* 2 (2013) 1322–1328.
- P.F.R. Ortega, Z. González, C. Blanco, R.L. Lavall, G.G. Silva, R. Santamaría, Biliquid supercapacitors: a simple and new strategy to enhance energy density in asymmetric/hybrid devices, *Electrochim. Acta* 54 (2017) 384–392.
- M. Pinzón, O. Aviles-García, A.R. de la Osa, A. de Lucas-Consuegra, P. Sanchez, A. Romero, New catalysts based on reduced graphene oxide for hydrogen production from ammonia decomposition, *Sustain. Chem. Pharm.* 25 (2022) 100615.
- C. Tewari, B. SanthiBhushan, A. Srivastava, N.G. Sahoo, Metal doped graphene oxide derived from quercus ilex fruits for selective and visual detection of iron(III) in water: experiment and theory, *Sustain. Chem. Pharm.* 21 (2021) 100436.
- U. Sierra, P. Álvarez, C. Blanco, M. Granda, R. Santamaría, R. Menéndez, New alternatives to graphite for producing graphene materials, *Carbon* 93 (2015) 812–818.
- B. Machado, P. Serp, Graphene-based materials for catalysis, *Catal. Sci. & Technol.* 2 (2012) 54–75.
- P. Sudarsanam, R. Zhong, S. Van den Bosch, S.M. Coman, V.I. Parvulescu, B.F. Sels, Functionalised heterogeneous catalysts for sustainable biomass valorisation, *Chem. Soc. Rev.* 47 (2018) 8349–8402.
- B. Sánchez-Page, M.V. Jiménez, J.J. Pérez-Torrente, V. Passarelli, J. Blasco, G. Subías, M. Granda, P. Álvarez, Hybrid Catalysts Comprised of Graphene Modified with Rhodium-Based N-Heterocyclic Carbenes for Alkyne Hydrosilylation, *ACS Applied Nano Materials* 3 (2020) 1640–1655.
- L. Zhao, B. Wang, R.A. Wang, Critical Review on New and Efficient 2D Materials for Catalysis, *Adv. Mater. Interfaces* 9 (2022) 2200771.
- L. Zhang, G. Zhou, Coordination engineering of single-atom copper embedded graphene-like borocarbonitrides for hydrogen production, *Appl. Surf. Sci.* 610 (2023) 155506.
- L. Jin, C. Liu, D. Wang, M. Liu, T.G. Lee, S.G. Peera, X. Qi, CdN4C0-gra as efficient trifunctional electrocatalyst for the HER, OER and ORR: A density functional theory study, *Appl. Surf. Sci.* 610 (2023) 155580.
- S. Cao, Y. Liu, T. Bo, R. Xu, N. Mu, W. Zhou, Prediction of functionalized graphene as potential catalysts for overall water splitting, *Appl. Surf. Sci.* 578 (2022) 151989.
- L. Li, P. Wang, Q. Shao, X. Huang, Recent progress in advanced electrocatalyst design for acidic oxygen evolution reaction, *Adv. Mater.* 33 (2021) 1–24.
- J. Li, R. Güttinger, R. More, F. Song, W. Wan, G.R. Patzke, Frontiers of water oxidation: the quest for true catalysts, *Chem. Soc. Rev.* 46 (2017) 6124–6147.
- R. Cao, W. Lai, P. Du, Catalytic water oxidation at single metal sites, *Energy Environ. Sci.* 5 (2012) 8134–8157.
- C. Meng, T. Ling, T.-Y. Ma, H. Wang, Z. Hu, Y. Zhou, J. Mao, X.W. Du, M. Jaroniec, S.Z. Qiao, Atomically and electronically couples Pt and CoO hybrid nanocatalysts for enhanced electrocatalytic performance, *Adv. Mater.* 29 (2017) 1–7.
- M. Tahir, N. Mahmood, J. Zhu, A. Mahmood, F.K. Butt, S. Rizwan, I. Aslam, M. Tanveer, F. Idrees, I. Shakir, C. Cao, Y. Hou, One dimensional graphitic carbon nitrides as effective metal-free oxygen reduction catalysts, *Sci. Rep.* 5 (2015) 1–10.
- M. Gong, Y. Li, H. Wang, Y. Liang, J.Z. Wu, J. Zhou, J. Wang, T. Regier, F. Wei, H. Dai, An advanced Ni-Fe layered double hydroxide electrocatalyst for water oxidation, *J. Am. Chem. Soc.* 135 (2013) 8452–8455.
- Z. Xia, Hydrogen evolution: Guiding principles, *Nat. Energy.* 1 (2016) 1–2.
- M. Tahir, L. Pan, F. Idrees, X. Zhang, L. Wang, J. Zou, Z.L. Wang, Electrocatalytic oxygen evolution reaction for energy conversion and storage: a comprehensive review, *Nano Energy* 37 (2017) 136–157.
- H.G. Sánchez-Casalouge, M.L. Ng, S. Kaya, D. Friebel, H. Ogasawara, A. Nilsson, In situ observation of surface species on iridium oxide nanoparticles during the oxygen evolution reaction, *Angew. Chem. Int. Ed.* 53 (2014) 7169–7172.
- A. Llobet, Molecular water oxidation catalysis: a key topic for new sustainable energy conversion schemes, John Wiley & Sons, Chichester, UK, 2014, pp. 29–134.
- T. Qiu, Z. Liang, M. Guo, S. Gao, C. Qu, H. Tabassum, H. Zhang, B. Zhu, R. Zou, Y. Shao-Horn, Highly exposed ruthenium-based electrocatalysts from bimetallic metal-organic frameworks for overall water splitting, *Nano Energy* 58 (2019) 1–10.
- J.D. Blakemore, R.H. Crabtree, G.W. Brudvig, Molecular catalysts for water oxidation, *Chem. Rev.* 115 (2015) 12974–13005.
- J.J. Concepcion, J.W. Jurss, M.K. Brennaman, P.G. Hoertz, A.O.T. Patrocínio, N. Y. Murakami Iha, J.L. Templeton, T.J. Meyer, Making oxygen with ruthenium complexes, *Acc. Chem. Res.* 42 (2009) 1954–1965.
- S. Fukuzumi, J. Jung, Y. Yamada, T. Kojima, W. Nam, Homogeneous and heterogeneous photocatalytic water oxidation by persulfate, *Chem. Asian J.* 11 (2006) 1138–1150.
- S. Zhan, M.S. Ahlquist, Dynamics and reactions of molecular Ru catalysts at carbon nanotube-water interfaces, *J. Am. Chem. Soc.* 140 (2018) 7498–7503.
- R. Mathew, I.A. Moreno-Hernandez, X. Sala, H.B. Gray, B.S. Brunshwig, A. Llobet, N.S. Lewis, Photoelectrochemical behavior of a molecular Ru-based water-oxidation catalyst bound to TiO<sub>2</sub>-protected Si photoanodes, *J. Am. Chem. Soc.* 139 (2017) 11345–11348.
- J. Nieto, M.V. Jiménez, P. Álvarez, A.M. Pérez-Mas, Z. González, R. Pereira, B. Sánchez-Page, J.J. Pérez-Torrente, J. Blasco, G. Subías, M. Blanco, R. Menéndez, Enhanced chemical and electrochemical water oxidation catalytic activity by hybrid carbon nanotube-based iridium catalysts having sulfonate-functionalized NHC ligands, *ACS Appl. Energy Mater.* 2 (2019) 3283–3296.
- Q. Shi, C. Zhu, D. Du, Y. Lin, Robust noble metal-based electrocatalysts for oxygen evolution reaction, *Chem. Soc. Rev.* 48 (2019) 3181–3192.
- H. Li, S. Di, P. Niu, S. Wang, J. Wang, Li Li, A durable half-metallic diatomic catalyst for efficient oxygen reduction, *Energy Environ. Sci.* 15 (2022) 1601–1610.
- H. Wang, X. Liu, P. Niu, S. Wang, J. Shi, L. Li, Porous Two-Dimensional Materials for Photocatalytic and Electrocatalytic Applications, *Matter.* 2 (2020) 1377–1413.
- Y. Wang, P. Niu, J. Li, S. Wang, L. Li, Recent progress of phosphorus composite anodes for sodium/potassium ion batteries, *Energy Storage Mater.* 3 (2021) 436–460.
- D.C. Marcano, D.V. Kosynkin, J.M. Berlin, A. Sinitskii, Z. Sun, A. Slesarev, L. B. Alemany, W. Lu, J.M. Tour, Improved synthesis of graphene oxide, *ACS Nano* 4 (2010) 4806–4814.
- D.R. Dreyer, S. Park, C.W. Bielawski, R.S. Ruoff, The chemistry of graphene oxide, *Chem. Soc. Rev.* 39 (2010) 228–240.
- J. Gao, F. Liu, Y. Liu, N. Ma, Z. Wang, X. Zhang, Environment-friendly method to produce graphene that employs vitamin C and amino acid, *Chem. Mater.* 22 (2010) 2213–2218.
- S. Park, R.S. Ruoff, Chemical methods for the production of graphenes, *Nat. Nanotechnol.* 4 (2009) 217–224.
- J. Coleman, Liquid exfoliation of defect-free graphene, *Acc. Chem. Res.* 46 (2013) 14–22.
- S. Lee, S.H. Eom, J.S. Chung, S.H. Hur, Large-scale production of high-quality reduced graphene oxide, *Chem. Eng. J.* 233 (2013) 297–304.
- U. Sierra, P. Álvarez, C. Blanco, M. Granda, R. Santamaría, R. Menéndez, Cokes of different origin as precursors of graphene oxide, *Fuel* 166 (2016) 400–403.
- C. Botas, P. Álvarez, P. Blanco, M. Granda, C. Blanco, R. Santamaría, L. J. Romasanta, R. Verdejo, M.A. López-Manchado, R. Menéndez, Graphene materials with different structures prepared from the same graphite by the Hummers and Brodie methods, *Carbon* 65 (2013) 156–164.
- C. Botas, P. Álvarez, C. Blanco, R. Santamaría, M. Granda, M.D. Gutiérrez, F. Rodríguez-Reinoso, R. Menéndez, Critical temperatures in the synthesis of graphene-like materials by thermal exfoliation-reduction of graphite oxide, *Carbon* 52 (2013) 476–485.
- C. Botas, P. Álvarez, C. Blanco, R. Santamaría, M. Granda, P. Ares, F. Rodríguez-oxide, The effect of the parent graphite on the structure of graphene oxide, *Carbon* 50 (2012) 275–282. <https://doi.org/10.1016/j.carbon.2011.08.045>.
- X. Fan, G. Zhang, F. Zhang, Multiple roles of graphene in heterogeneous catalysis, *Chem. Soc. Rev.* 44 (2015) 3023–3035.
- M.R. Axet, J. Durand, M. Gouygon, P. Serp, Surface coordination chemistry on graphene and two-dimensional carbon materials for well-defined single atom supported catalysts, *Adv. Organomet. Chem.* 71 (2019) 53e174.
- B. Sánchez-Page, A.M. Pérez-Mas, M. González-Ingelmo, L. Fernández, Z. González, M.V. Jiménez, J.J. Pérez-Torrente, J. Blasco, G. Subías, P. Álvarez, M. Granda, R. Menéndez, Influence of graphene sheet properties as supports of iridium-based N-heterocyclic carbene hybrid materials for water oxidation electrocatalysis, *J. Organomet. Chem.* 919 (2020) 121334.
- X. Zhu, G. Wu, Y. Li, W. Wang, J. Wang, W. Yang, Heterojunction photocatalysts formed by reduced graphene oxide derived from defective spent cathode carbon and ZnIn<sub>2</sub>S<sub>4</sub> for boosting photocatalytic hydrogen evolution, *Sustain. Chem. Pharm.* 33 (2023) 101118.
- P. Fortgang, T. Tite, V. Barnier, N. Zehani, C. Maddi, F. Lagarde, A. Loir, N. Jaffrezic-Renault, C. Donnet, F. Garrelie, C. Chaix, Robust Electrografting on self-organized 3D graphene electrodes, *ACS Appl. Mater. Interfaces* 8 (2016) 1424–1433.
- R. Usón, L.A. Oro, J.A. Cabeza, Dinuclear methoxy, cyclooctadiene, and barrelene complexes of rhodium(I) and iridium(I), *Inorg. Synth.* 23 (1985) 126–130.
- L. Fernández-García, P. Álvarez, A. Pérez-Mas, C. Blanco, R. Santamaría, R. Menéndez, M. Granda, Peculiarities of the production of graphene oxides with controlled properties from industrial coal liquids, *Fuel* 203 (2017) 253–260.
- W.S. Hummers, R.E. Offeman, Preparation of graphitic oxide, *J. Am. Chem. Soc.* 80 (1958) 1339.

- [60] P.M.A. Sherwood, In: D. Briggs, M. P. Seah (eds.), 1990. *Practical Surface Analysis in Auger and X-ray Photoelectron Spectroscopy*, Wiley: New York, 2nd ed., vol. 1, 657.
- [61] D. Elgrabli, M. Floriani, S. Abella-Gallar, L. Meunier, C. Gamez, P. Delalain, F. Rogerieux, J. Boczkowski, G. Lacroix, Biodistribution and clearance of instilled carbon nanotubes in rat lung, Part. Fibre. Toxicol. 5 (2008) 20–33.
- [62] L. Simonelli, C. Marini, W. Olszewski, M. Ávila Pérez, N. Ramanan, G. Guilera, V. Cuartero, K. Klementiev, CLÆSS: the hard x-ray absorption beamline of the ALBA CELLS synchrotron, Cogent Physics 3 (2016) 1231987.
- [63] B. Ravel, M. Newville, Athena, artemis, hephaestus: data analysis for X-ray absorption spectroscopy using IFEFFIT, J. Synchrotron Radiat. 12 (2005) 537–541.
- [64] J.J. Rehr, R.C. Albers, Theoretical approaches to X-ray absorption fine structure, Rev. Mod. Phys. 72 (2000) 621–654.
- [65] Z. González, B. Acevedo, G. Predeanu, S.M. Axinte, M.F. Drăgoescu, V.V. Slăvescu, J.J. Fernandez, M. Granda, G. Gryglewicz, S. Melendi-Espina, Graphene materials from microwave-derived carbon precursors, Fuel Process. Technol. 217 (2021) 106803.
- [66] H.C. Schniepp, J.L. Li, M.J. McAllister, H. Sai, M. Herrera-Alonso, D.H. Adamson, R.K. Prud'homme, R. Car, D.A. Saville, I.A.J. Aksay, Functionalized single graphene sheets derived from splitting graphite oxide, Phys. Chem. B 110 (2006) 8535–8539.
- [67] C. Hontoria-Lucas, A.J. López-Peinado, J.D. López-González, M.L. Rojas-Cervantes, R.M. Martín-Aranda, Study of oxygen-containing groups in a series of graphite oxides: Physical and chemical characterization, Carbon 33 (1995) 1585–1592.
- [68] A. Ganguly, S. Sharma, P. Papakonstantinou, J. Hamilton, Probing the thermal deoxygenation of graphene oxide using high-resolution in situ X-ray-based spectroscopies, J. Phys. Chem. C 115 (2011) 17009–17019.
- [69] M. Blanco, P. Álvarez, C. Blanco, M.V. Jiménez, J. Fernández-Tornos, J.J. Pérez-Torrente, L.A. Oro, R. Menéndez, Enhanced hydrogen-transfer catalytic activity of iridium N-heterocyclic carbenes by covalent attachment on carbon nanotubes, ACS Catal. 3 (2013) 1307–1317.
- [70] C. Crotti, E. Farnetti, S. Filipuzzi, M. Stener, E. Zangrando, P. Moras, Evaluation of the donor ability of phenanthrolines in iridium complexes by means of synchrotron radiation photoemission spectroscopy and DFT calculations, Dalton Trans. 1 (2007) 133–142.
- [71] M. Blanco, P. Álvarez, C. Blanco, M.V. Jiménez, J. Fernández-Tornos, J.J. Pérez-Torrente, L.A. Oro, R. Menéndez, Graphene-NHC-iridium hybrid catalysts built through -OH covalent linkage, Carbon 83 (2015) 21–31.
- [72] F.W. Lytle, P.S.P. Wei, R.B. Gregor, G.H. Via, J.H. Sinfelt, Effect of chemical environment on magnitude of x-ray absorption resonance at LIII edges. Studies on metallic elements, compounds, and catalysts, J. Chem. Phys. 70 (1979) 4849–4855.
- [73] M. Blanco, P. Álvarez, C. Blanco, M.V. Jiménez, J. Fernández-Tornos, J.J. Pérez-Torrente, J. Blasco, G. Subías, V. Cuartero, L.A. Oro, R. Menéndez, Effect of structural differences of carbon nanotubes and graphene based iridium-NHC materials on the hydrogen transfer catalytic activity, Carbon 96 (2016) 66–74.